Numerical Study on Water Entry of Projectiles with Various Head Shapes by a Multiphase Moving Particle Semi-implicit Method

Ruosi Zha*
School of Ocean Engineering and Technology, Sun Yat-Sen University
Zhuhai, Guangdong, China

Weiwen Zhao* and Decheng Wan*†
Computational Marine Hydrodynamic Lab, School of Naval Architecture, Ocean and Civil Engineering
Shanghai Jiao Tong University, Shanghai, China

In this paper, the low-speed water entry of four projectiles with various head types is numerically studied by using an improved multiphase moving particle semi-implicit (MPS) method. The projectiles are composed of a solid circular cylinder with $L/D = 4.5$ and different head shapes, including a hemispherical head and three cone-shaped heads (90°∼150°). During the water entry of these free-falling projectiles, splashing water, the deformed free surface, and the cavity evolution behind the cylinder are presented, which show agreement with experimental data. The vertical velocities and forces obtained by the multiphase MPS method are given. The influences of varying head shapes on the motion of the projectiles and the generation and closure of cavities are analyzed.

INTRODUCTION

There widely exist water entry phenomena in the defense industry and ocean engineering with a fluid-structure interaction and multiphase flow. Water entry by a projectile involving cavity formation and collapse has been investigated theoretically. For example, Lee et al. (1997) developed an analytical model for the cavity dynamics to study the high-speed water entry of a sphere. It was indicated that a cavity can be characterized as a deep closure prior to closure at the surface for high-speed water entry, and the time of deep closure was constant, which was independent of the impact velocity. Mirzaei et al. (2020) proposed a transient model to predict the shape of the oblique water entry cavity for a cylindrical projectile at different angles. The predicted projectile attitude and the trajectory of the projectile agreed well with the experimental data.

Experimental studies on both low-speed and high-speed water entry with cavities have also been extensively carried out by using high-speed cameras. For example, Truscott and Techet (2009a, 2009b) and Techet and Truscott (2011) experimentally studied the trajectories, forces, and cavity formation behind spinning hydrophobic and hydrophilic spheres after water entry in the MIT Experimental Hydrodynamics Laboratory at the Massachusetts Institute of Technology. The splash and cavity of spheres' water entry with varying spin rates and impact velocities were compared. Yang et al. (2014) conducted a series of experiments of low-speed water entry of projectiles with different head types. The snapshots of the cavity-running phase under different velocity and entry angle conditions were recorded by high-speed photography, and the influences of head types on the characteristics of cav-

ity formation and closure were analyzed. The oblique high-speed water entry of projectiles was investigated by Song et al. (2020). The deflection of trajectories and the evolution of supercavities were analyzed.

Over the past decades, numerical simulations of water entry have been performed based on the computational fluid dynamics (CFD) method. Among mesh-based CFD methods, the volume of fluid method is one of the most popular methods to capture the free surface for simulating the multiphase flows. For example, Song et al. (2020) adopted the commercial software STAR-CCM+ to study the cavity of water entry for projectiles at an oblique speed. Overset mesh techniques and the dynamic fluid body interaction method were employed to resolve the motion of projectiles. Pressure distributions on the nose of projectiles were analyzed at different entry angles. Jiang et al. (2021) studied pairs of supersonic projectiles entering the water in series and in parallel by solving the compressible Reynolds-averaged Navier–Stokes equations. In this work, different head shapes, entry velocities, interval times, and interval distances were discussed for their influences on the drag force coefficient and cavity evolution.

However, it is still challenging to accurately simulate the water splashing with a large deformation of the free surface and the motion of moving boundaries with a large amplitude by using mesh-based methods during water entry. The Lagrangian particle-based methods are mesh-free, which have advantages in solving water entry problems, especially with highly deformed interfaces and moving boundaries. Among the Lagrangian particle methods, the smoothed particle hydrodynamics (SPH) method (Monaghan, 1988) for weakly compressible flows, the moving particle semi-implicit (MPS) method (Koshizuka and Oka, 1996) for incompressible flows, and many improved SPH/MPS methods to deal with the numerical issues in the original methods have been developed in recent years. Various improvements and applications of particle methods to the fluid-structure interaction problems can be found in the review works of Liu and Zhang (2019), Luo et al. (2021), Gotoh et al. (2021), and Zhang et al. (2022).

Difficulties still exist in treating the cavity and its interaction with the structure and the fluid. To solve this problem, multiphase models for mesh-free methods have also been developed to

address the air phase including cavity and cavitation. The employment of the surface tension leads to an improvement in the simulations of the interface between two-phase flows. For example, Gong et al. (2011) successfully employed the two-phase SPH method to simulate the water entry and enclosing of a wedge. The air entrapment and jet flow were observed, and the two-phase SPH model was validated by comparing the results with experimental data. Multiphase and strongly compressible flows with large volume variations were simulated by developing an improved δ-SPH (Sun et al., 2020a, 2020b). The energy equation was coupled with the momentum equation and solved to deal with the strong compressibility of the fluid. The multiphase SPH method can be successfully employed to simulate cavitation bubbles and underwater explosion bubbles. Rezavand et al. (2019) developed a weakly compressible SPH method based on a low-dissipation Riemann solver and the transport-velocity formulation and applied it to simulate violent multiphase flows with a high-density ratio. In terms of the MPS method, the surface tension models (Nomura et al., 2001; Khayyer and Gotoh, 2013, 2016; Duan et al., 2015) were proposed for treating the interface of multiphase flows. A stable multiphase MPS method was developed by Duan et al. (2017) in which the continuities of acceleration and velocity fields can be fully guaranteed. Numerical instability was overcome by incorporating the concept of space potential particles in the work of Shimizu et al. (2018) for multiphase flows with high density ratios. Khayyer et al. (2017, 2019) developed the optimized particle shifting scheme based on the incompressible SPH method to avoid particle penetrations for multiphase simulations; thus, the stability of the interface was enhanced. Recently, a multiphase MPS method was developed by introducing multiphase models into the single-phase improved MPS in the work of Wen et al. (2021a, 2021b, 2022). The numerical stability and accuracy of this multiphase MPS method have been verified and validated by applying it to simulations of two-dimensional (2-D)/three-dimensional (3-D) bubbly flows and violent interfacial flows with complex interfaces. The interaction between different fluids with a high-density ratio and a high viscosity ratio can be simulated.

In the present work, the improved multiphase MPS method was applied to solve water entry problems. Numerical studies were carried out for the perpendicular water entry of projectiles with four head shapes at a low entry speed. Numerical results including the vertical velocity of projectiles, impact forces, and the cavity and free surface are presented. The influence of the head shape on the cavity dynamics is also discussed based on the numerical results.

NUMERICAL METHOD

Based on the improved MPS method (Zhang and Wan, 2017), the multiphase models are further developed including the particle interaction model with an improved gradient model and an improved Laplacian model, a continuous acceleration model, a surface tension model, and a multiphase collision model (Wen et al., 2021a, 2021b). The surface tension can be accurately computed by using the contoured continuum surface force (CCSF) model to calculate the interface curvature. The body motion during the water entry is simulated by solving the six-degrees-of-freedom equations of motion. The pressure Poisson equations were improved by introducing an incompressible-compressible model in the source term to consider the compressibility of the air phase in the cavity.

Governing Equations

The governing equations including the continuity equation and the momentum equations in the multiphase MPS particle method are written as

$$\frac{1}{\rho}\frac{D\rho}{Dt} = -\nabla \cdot \boldsymbol{u} \tag{1}$$

$$\rho\frac{D\boldsymbol{u}}{Dt} = -\nabla P + \mu\nabla \cdot \nabla \boldsymbol{u} + \boldsymbol{F^B} + \boldsymbol{F^S} \tag{2}$$

where ρ, $\boldsymbol{u}$, P, μ, $\boldsymbol{F^B}$, and $\boldsymbol{F^S}$ are the density, velocity, pressure, dynamic viscosity, body force, and surface tension force, respectively, on fluid. Note that the governing equations for fluids with different phases are solved simultaneously. In addition, the multidensity and multiviscosity models are employed for multiphase simulations. The density smoothing scheme is adopted to smooth the transition of density field across the interface between the multiphases with a high-density ratio. The smoothed density of a particle can be obtained by

$$\langle\rho\rangle_i = \frac{\rho_i W_{self} + \sum_{j\in I}\rho_j W_{ij}}{W_{self} + \sum_{j\in I}W_{ij}} \tag{3}$$

where i represents the target particle, and j stands for its neighboring particles in the region I; $\langle\rangle$ denotes the approximation of a variable in the interaction region of a particle. W_{ij} is the kernel function defined by

$$W_{ij} = \begin{cases} \dfrac{r_e}{0.85r_{ij} + 0.15r_e} - 1 & 0 \le r_{ij} < r_e, \\ 0 & r_e \le r_{ij}, \end{cases} \tag{4}$$

where r_{ij} and r_e are the distance between two particles and the radius of the interaction region, respectively. W_{self} is used to amplify the effect of the target particle itself, defined as $W_{self} = n^0$. n^0 is the initial particle number density, n_i, which is defined as the sum of kernel functions of particles within the interaction region of a particle i.

$$n_i = \sum_{j\ne i}W_{ij} \tag{5}$$

The interparticle viscosity model is employed to obtain an accurate viscous force between particles of two phases. The viscous force can be obtained by

$$\mu\nabla \cdot \nabla \boldsymbol{u} = \frac{2d}{n^0\lambda}\sum_{j\ne i}\frac{2\mu_i\mu_j}{\mu_i + \mu_j}(\boldsymbol{u}_j - \boldsymbol{u}_i)W_{ij} \tag{6}$$

where d is the number of spatial dimensions, and λ is a parameter calculated as follows.

$$\lambda = \frac{\sum_{j\ne i}W_{ij}r_{ij}^2}{\sum_{j\ne i}W_{ij}} \tag{7}$$

Particle Interaction Models

The continuous acceleration model (Duan et al., 2017) is introduced to deal with the high discrepancy of particle accelerations across the phase interfaces. The gradient operator can be calculated as the weighted average gradient of all neighboring particles with the interparticle density in the interaction region:

$$\left\langle\frac{2}{\rho_i + \rho_j}\nabla P\right\rangle_i = \frac{d}{n^0}\sum_{j\ne i}\left[\frac{2(P_j - P_i)}{\rho_i + \rho_j}\frac{\boldsymbol{r}_j - \boldsymbol{r}_i}{|\boldsymbol{r}_j - \boldsymbol{r}_i|^2}W_{ij}\right]$$

$$+\frac{d}{n^0}\sum_{j\neq i}\left[\frac{\left(P_i - P'_{i,\min}\right)}{\rho_i}\frac{\boldsymbol{r}_j - \boldsymbol{r}_i}{\left|\boldsymbol{r}_j - \boldsymbol{r}_i\right|^2}W_{ij}\right] \qquad (8)$$

where P_i and P_j are pressures of particle i at $\boldsymbol{r}_i$ and of the neighboring particle j at $\boldsymbol{r}_j$, respectively. Note that $P'_{i,\min}$ is the minimum pressure among the neighbouring particles of the target particle i with the identical phase. The first term is the original pressure gradient model with the interparticle density, and the other term is a particle-stabilizing term to improve the distribution of particles artificially.

In the present work, the original divergence model and Laplacian model (Koshizuka and Oka, 1996) were also rewritten with the interparticle density to compute the divergence and Laplacian of a variable ϕ.

$$\left\langle\frac{2}{\rho_i + \rho_j}\nabla\cdot\boldsymbol{\phi}\right\rangle_i = \frac{d}{n^0}\sum_{j\neq i}\frac{2\left(\boldsymbol{\phi}_j - \boldsymbol{\phi}_i\right)}{\rho_i + \rho_j}\cdot\frac{\boldsymbol{r}_j - \boldsymbol{r}_i}{\left|\boldsymbol{r}_j - \boldsymbol{r}_i\right|^2}W_{ij} \qquad (9)$$

$$\left\langle\frac{2}{\rho_i + \rho_j}\nabla^2\phi\right\rangle_i = \frac{2d}{n^0\lambda}\sum_{j\neq i}\frac{2}{\rho_i + \rho_j}\left(\phi_j - \phi_i\right)W_{ij} \qquad (10)$$

Pressure Poisson Equation

The pressure Poisson equations (PPEs) can be derived by implicitly correcting the particle-number density to the initial value n^0. The divergence free of velocity is also applied in the source term to suppress the pressure fluctuations in the numerical results with the original MPS method. The improved PPE with a mixed source term (Lee et al., 2011; Zhang and Wan, 2017) is written as

$$\langle\nabla^2 P^{k+1}\rangle_i = (1-\gamma)\frac{\rho}{\Delta t}\nabla\cdot\boldsymbol{u}_i^* - \gamma\frac{\rho}{\Delta t^2}\frac{\langle n^k\rangle_i - n^0}{n^0} \qquad (11)$$

where γ is a blending parameter, which is set as 0.01 in this work. Based on Eq. 11, an incompressible-compressible model is used by introducing the compressible term derived from equation of state. Finally, the PPE for multiphase MPS (Wen et al., 2021b; Khayyer and Gotoh, 2022) is derived as

$$\langle\nabla^2 P^{k+1}\rangle_i = (1-\gamma)\frac{\rho}{\Delta t}\nabla\cdot\boldsymbol{u}_i^* - \gamma\frac{\rho}{\Delta t^2}\frac{\langle n^k\rangle_i - n^0}{n^0}$$
$$+\frac{1}{\Delta t^2 C_s^2}\left(P_i^{k+1} - P_i^k\right) \qquad (12)$$

where C_s denotes the speed of sound. After divided by ρ for both sides of Eq. 12, an arithmetic mean density of particle is used to the Laplacian term in the PPE to improve the particle calculations for fluids with a high density ratio.

$$\rho = \frac{\rho_i + \rho_j}{2} \qquad (13)$$

Surface Tension Model

For the cavity evolution, it is important to consider the surface tension force on the interface between the multiphase fluids. In this work, the surface tension model in combination with the continuum surface force (CSF) model was employed (Wen et al., 2021b). In the CSF model, the surface tension force is calculated as a body force exerted on particles in the transition region. The transition region is defined as a region in which there are particles of different phases inside the interaction region of a particle near the interface. The value of surface tension force is calculated by

$$\boldsymbol{F}^s = -\sigma\kappa\nabla C \qquad (14)$$

where σ, κ, and ∇C represent the surface tension coefficient of fluid, the interface curvature, and the gradient of color function, respectively. The color function is defined as

$$C_{ij} = \begin{cases} 0 & \text{if particles } i \text{ and } j \text{ belong to the same phase,} \\ 1 & \text{if particles } i \text{ and } j \text{ belong to different phases} \end{cases} \qquad (15)$$

However, it could lead to a discontinuity of the acceleration field near the interface of different phases because of a high-density ratio of fluids. To solve this problem, an improved color function is used.

$$C_{ij} = \begin{cases} 0 & \text{if particles } i \text{ and } j \text{ belong to} \\ & \quad \text{the same phase,} \\ \dfrac{2\rho_i}{\rho_i + \rho_j} & \text{if particles } i \text{ and } j \text{ belong} \\ & \quad \text{to different phases} \end{cases} \qquad (16)$$

The CCSF model is employed to calculate the interface curvature, κ. For 2-D simulations, the interface curvature is derived as

$$\kappa = \frac{y''}{(1+y_i')^{3/2}} = \frac{2f_{x,i}f_{y,i}f_{xy,i} - f_{x,i}^2 f_{yy,i} - f_{y,i}^2 f_{xx,i}}{\left(f_{x,i}^2 + f_{y,i}^2\right)^{3/2}} \qquad (17)$$

where $f(x, y)$ is the smoothed color function at an arbitrary location (x, y), which can be calculated according to the Gaussian kernel function and the smoothed radius of a particle. Details can be found in the work by Duan et al. (2015) and Wen et al. (2021a).

Multiphase Collision Model

To overcome the nonphysical penetrations between different phases of fluids, the multiphase collision model (Shakibaeinia and Jin, 2012) was adopted to generate a repulsive force to keep particles from getting too close. If the distance between any two particles is below a certain threshold (e.g., $0.8l_0$), the collision model would take effect to improve the numerical stability, and the velocities of particles are then corrected according to

$$\boldsymbol{u}_i' = \boldsymbol{u}_i - \frac{1}{\rho_i}(1+\varepsilon)\frac{\rho_i\rho_j}{\rho_i + \rho_j}\boldsymbol{u}_{ij}^n \qquad (18)$$

$$\boldsymbol{u}_j' = \boldsymbol{u}_j + \frac{1}{\rho_j}(1+\varepsilon)\frac{\rho_i\rho_j}{\rho_i + \rho_j}\boldsymbol{u}_{ij}^n \qquad (19)$$

where $\boldsymbol{u}_i'$ and $\boldsymbol{u}_j'$ are the corrected velocities of two particles after collision, and ε is the collision ratio. In this work, $\varepsilon = 0.5$ is used for the velocity correction.

COMPUTATIONAL SETUP

Simulations of water entry of projectiles with different head shapes were carried out according to the experimental setups, which were conducted by Yang et al. (2014). The material of the projectile is aluminum, and the density of projectiles is therefore set as 2,700 kg/m³. The projectiles can be considered rigid bodies because of the low impact velocity during water entry. Free-fall motion of the body with one degree of freedom is investigated. One degree of freedom represents the translation toward the y axis in the vertical direction. No rotations are considered. Because the geometries of the projectile are symmetrical, we focus on the vertical motion in 2-D simulations. It can be imposed by using Newton's second law of motion. The projectiles are made of two parts, including the circular cylinder and the head. It should be noted that both the material and size of projectiles are generally the same excluding their head shapes. The total length and the
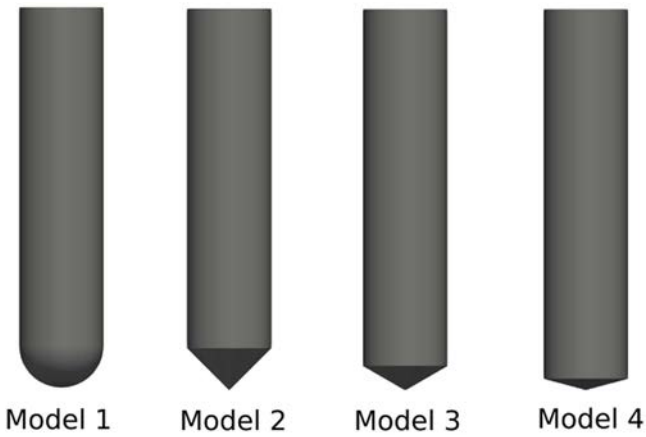
Fig. 1 Geometry of the projectiles with different head shapes

Fig. 3 Initial particle distributions for Model 1 with a particle spacing of 0.7×10^{-3} m and 512,443 particles

diameter of the circular cylinder are set as $L = 45$ mm and $D = 10$ mm, respectively. The head shapes are, namely, a hemispherical head, a 90° cone-shaped head, a 120° cone-shaped head, and a 150° cone-shaped head. The geometries (Models 1–4) are illustrated in Fig. 1.

The computational domain with the length L_d and the diameter of the cylinder D is shown in Fig. 2.

The nondimensional domain length $L_d/D = 40$ was chosen to avoid the wall effects. The height of the air phase was set as $H_a = 200$ mm, and the depth of water was set as $H_w = 400$ mm. The coordinate system was established on the initial free surface at the center of the domain. The tips of projectiles were set on the origin point instead of the location in experiments to save computational resources. Projectiles will fall vertically downward along the $-y$ direction. The initial drop velocity is equal to 3.13 m/s, according to the drop height from experimental setups. Boundary conditions are applied by using the one layer of boundary particles and two layers of dummy particles. The pressures on the first layer of boundary particles are calculated by solving the PPE, and those on the dummy particles are obtained by extrapolation. No-slip wall boundary conditions were implemented for the tank walls and the body surface. The velocity of the moving bound-
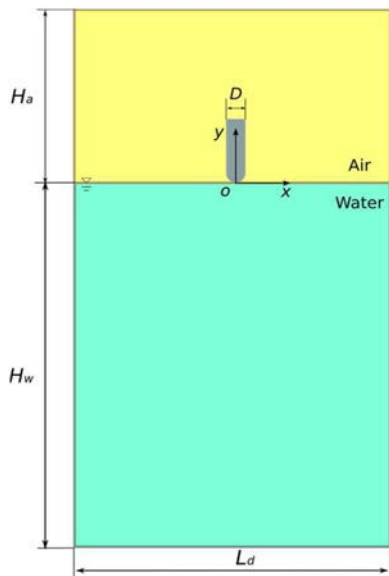
aries is obtained based on solving the motion equations of the rigid body. The forces on the rigid body can be obtained by integrating the pressures on wall particles. As an example of particle discretization, the wall particles of Model 1 and the fluid particles around it are shown in Fig. 3.

CORRECTIONS OF 2-D RESULTS

An important part of the discrepancies could result from the limitation of 2-D simulations. The surface area and mass of 2-D models were not the same as those for 3-D geometries. For example, for Model 1 with a hemispherical head, the vertical force is calculated by

$$F = \int p(x, y) \cdot \vec{n} \, dS \tag{20}$$

where p is the pressure on the body surface, $\vec{n}$ is the normal vector, and S is the surface area. For estimation, p is assumed to be uniformly distributed on the surface:

$$F_{2D} = \int p(x, y) \cdot \vec{n} \, dS = \sum p(x, y) \cdot D \cdot 1 \tag{21}$$

$$F_{3D} = \int p(x, y) \cdot \vec{n} \, dS = \sum p(x, y) \cdot \frac{\pi D^2}{4} \tag{22}$$

where D is the diameter of the cylinder. The mass of the projectile Model 1 is calculated as follows.

$$M_{2D} = M_{head} + M_{cylinder} = \rho \cdot \left(L \cdot D + \frac{\pi D^2}{2} \right) \tag{23}$$

$$M_{3D} = M_{head} + M_{cylinder} = \rho \cdot \left(L \cdot \frac{\pi D^2}{4} + \frac{\pi D^3}{12} \right) \tag{24}$$

Therefore, the ratio between the accelerations of 2-D and 3-D simulations can be estimated as follows.

$$a_{3D}/a_{2D} = \frac{F_{3D}}{M_{3D}} \Big/ \frac{F_{2D}}{M_{2D}} \approx \frac{(\pi D^2/4) \cdot (L \cdot D + \pi D^2/2)}{D \cdot [L \cdot (\pi D^2/4) + \pi D^3/12]} \tag{25}$$

To eliminate the inconsistency of 2-D simulations and experimental observations, an estimated correction on the body motion including the acceleration based on Eq. 23 was made. Note that this estimation belongs to preliminary results because only 2-D simulations are available; improved results should be adopted using 3-D simulations in future work. After corrections, the inconsistency can be avoided.

Fig. 2 Computational domain and coordinates for 2-D simulations

NUMERICAL RESULTS

Convergence Studies

Convergence studies of Model 1 with a hemispherical head at an impact velocity of 3.13 m/s were performed for verification. Convergence studies were first carried out on particle spacing with four particle resolutions in terms of $l_0 = 1.4 \times 10^{-3}$ m, 1.0×10^{-3} m, 0.85×10^{-3} m, and 0.7×10^{-3} m. The time step of 0.3×10^{-4} s was employed in these cases. The convergence of vertical velocity and impact force to particle spacing for Model 1 was presented in Figs. 4 and 5, respectively. It can be seen that the numerical results converged as the particle spacing was decreased. Finally, the particle spacing of 0.7×10^{-3} m was used in the following studies.

Convergence studies with four time steps were then carried out with $\Delta t = 0.5 \times 10^{-4}$ s, 0.4×10^{-4} s, 0.3×10^{-4} s, and 0.2×10^{-4} s. In these cases, the particle spacing was kept the same as in 0.7×10^{-3} m. The convergence of vertical velocity and impact force to the time step for Model 1 was presented in Figs. 6 and 7, respectively. It can be observed that the numerical results converged as the time step was decreased. The results are close if the time step was smaller than 0.3×10^{-4} s. Therefore, the time step of $\Delta t = 0.3 \times 10^{-4}$ s was employed in the present simulations.

Four cases were simulated by the multiphase MPS method. Based on the result of convergence studies, a summary of the case matrix is given in Table 1. At least 10 particles per diameter of the cylinder are needed to represent the geometrical details of head shapes. The total number of particles was almost 0.5 million for 2-D simulations. For the temporal discretization, the time step is determined by the CFL number, defined as $CFL = V_0 \cdot \Delta t / l_0$,
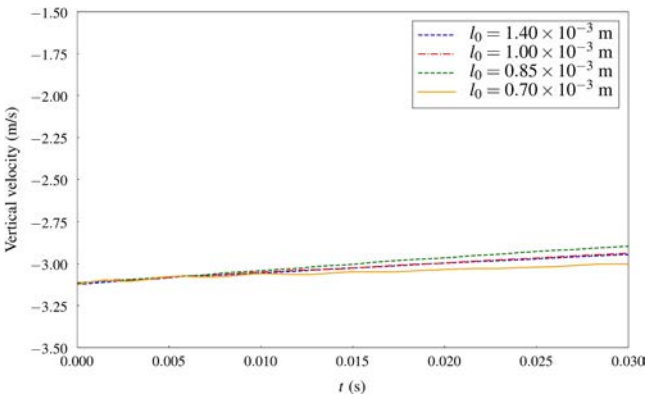
Fig. 4 Convergence of corrected vertical velocity to particle spacing for Model 1
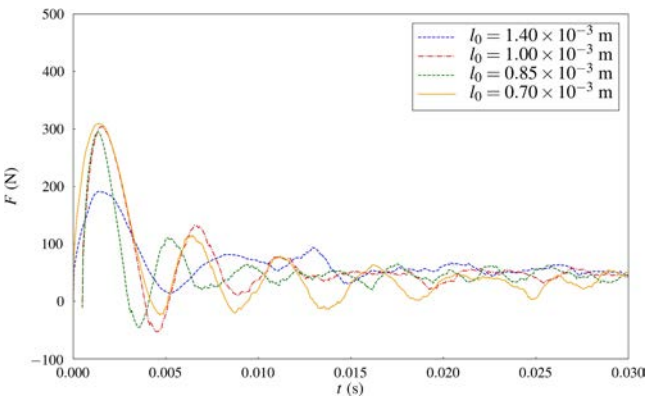
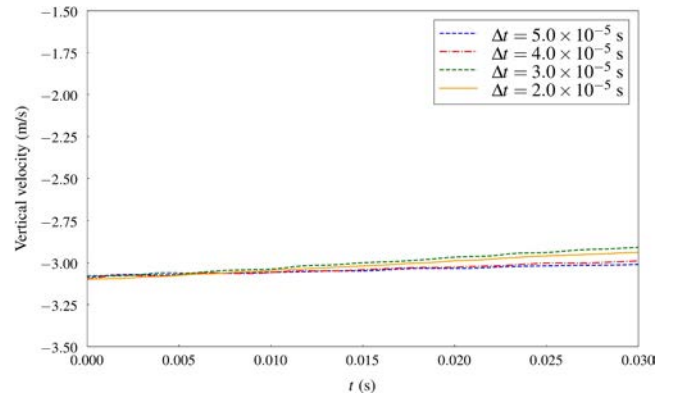Fig. 5 Convergence of impact force to particle spacing for Model 1

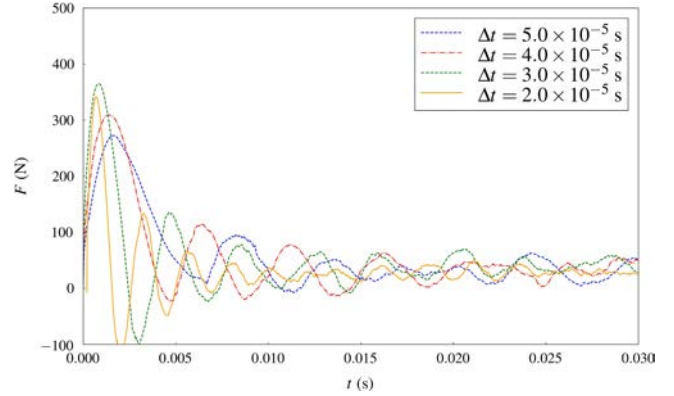Fig. 6 Convergence of vertical velocity to time step for Model 1

Fig. 7 Convergence of impact force to time step for Model 1

Item	Case 1	Case 2	Case 3	Case 4
Geometry	Model 1	Model 2	Model 3	Model 4
Particle number	512,443	512,469	512,457	512,447
Particle spacing (m)	0.7×10^{-3}	0.7×10^{-3}	0.7×10^{-3}	0.7×10^{-3}
Time step (s)	0.3×10^{-4}	0.3×10^{-4}	0.3×10^{-4}	0.3×10^{-4}

Table 1   Summary of the 2-D simulation cases

where V_0, Δt, and l_0 are the magnitude of the initial drop velocity, time step, and particle spacing, respectively. For all cases, $CFL = 0.14$ was employed for numerical accuracy and stability.

For the 2-D simulations of vertical projectiles entering calm water, numerical results including the vertical velocity, impact force on the body, free surface, and cavity evolution of four projectile models with different head shapes based on the multiphase MPS method are presented.

Vertical Velocity

Time histories of vertical velocities in Cases 1~4 are presented in Fig. 8. The velocities at $t = 0$ s represent the initial impact velocities, V_0, which were set as 3.13 m/s for all cases with the same drop height.

It can be observed that the vertical velocity magnitudes were decreased as the time was increased. For Case 1, the velocity magnitudes for the hemispherical head are greater than those for
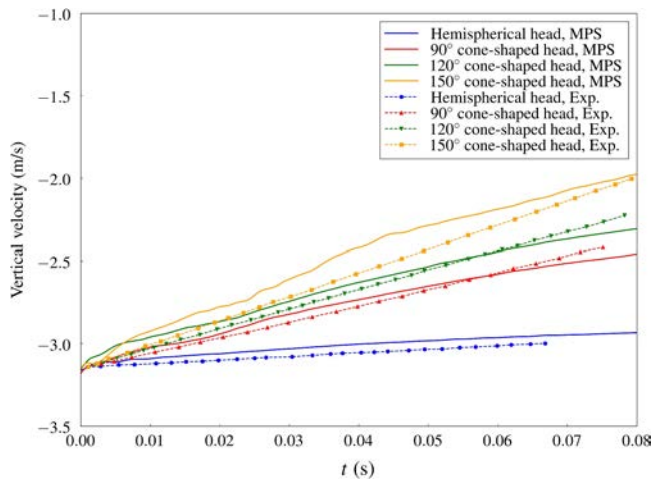
Fig. 8 Time histories of corrected vertical velocities for projectile models with four head shapes during water entry

the cone-shaped heads. For Cases 2–4, where the angle of cone-shaped head increased from 90° to 150°, the velocity magnitudes of those models decreased with a similar acceleration. The acceleration did not change too much in the range of $0.02 < t < 0.08$ s. However, the velocity loss for the projectile model with a hemispherical head in Case 1 is the lowest (50%), whereas that for the projectile model with a 150° cone-shaped head in Case 4 is the highest (66.7%) during water entry. This indicates a more significant change of velocity for the projectile model with a flatter head shape. In summary, the projectile with a cone-shaped head with a large angle can be decelerated a lot for the low-speed water entry process. According to the experimental data, the change of velocities for the projectile model with a flatter head shape was always larger.

Impact Force

Figure 9 shows the vertical impact forces exerted on projectile models with four head shapes in Cases 1~4. For $t < 0.002$ s, the impulsive impact force quickly raised up to the peak and then decreased before $t = 0.005$ s for all four curves. It would bring a high transient acceleration to slow down the projectiles in the water. The amplitude and time were affected by the head shape.
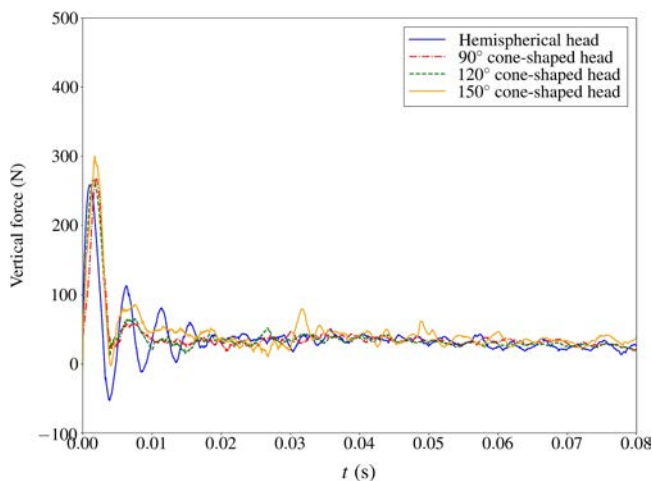

Fig. 9 Time histories of impact forces for projectile models with four head shapes during water entry

The rise time and decay time for the model with a hemispherical head in Case 1 were shorter than that for the models with cone-shaped heads in Cases 2–4. The vertical velocity of the model with a hemispherical head was therefore decreased the least. It can be observed that the peak value of the slamming force for the model with a 150° cone-shaped head was the greatest. After the impact, the vertical force for the model with a hemispherical head decreased with small oscillation and then decayed before $t = 0.02$ s.

For the range of $t > 0.02$ s, the amplitude of the vertical force remained unchanged when the projectiles entered the water totally. It can be observed that the projectile models with cone-shaped heads of different angles were subject to a similar vertical force after they were immersed in the water. It can be summarized that the shape of projectile heads mainly had a significant impact on the slamming loads during the slamming time and had little influence on the slamming loads after the projectile models were immersed. The projectile model with a large angle cone-shaped head was subjected to a higher impact force than those with a hemispherical head or a cone-shaped head with a small angle.

Free Surface and Cavity

The characteristics of cavity flow for the projectile models with different head shapes were mainly investigated. The free surface and cavity at five typical instants ($t = 0.002, 0.012, 0.022, 0.032,$ and 0.042 s in experiments) for the projectile model with a hemispherical head in Case 1 are shown in Fig. 10. The left side of each panel is a snapshot of the experiment (Yang et al., 2014), and the right side shows the numerical results. Little splashing water was observed at $t = 0.002$ s, and no cavities were formed during the head entering the water before $t = 0.012$ s. Afterward, bubbles were formed above the bottom of the cylinder. The width of the bubble was equal to the diameter of the cylinder. With the projectile model entering the water in depth, the length of the cavity was increased while the width of that remained nearly constant at
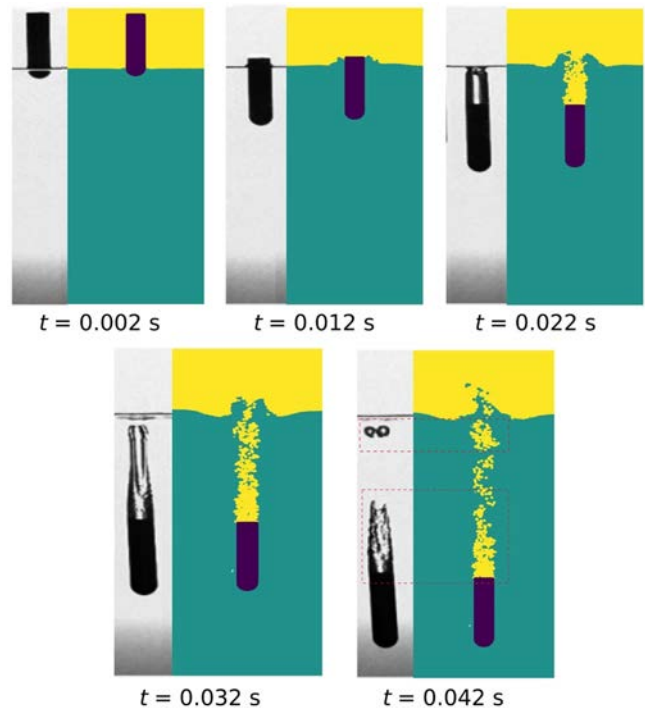

Fig. 10 Typical cavity geometries and free surface during water entry of Model 1 with a hemispherical head
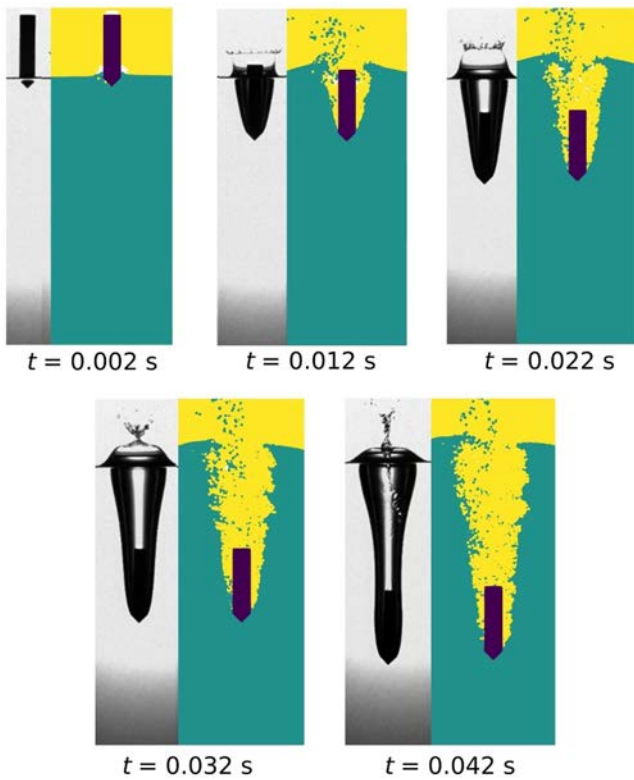
Fig. 11 Typical cavity geometries and free surface during water entry of Model 2 with a 90° cone-shaped head

bubble was still as wide as the cylinder. Cavity surface closure was observed, and bubbles were detached at $t = 0.032$ s. Finally, smaller bubbles were generated and raised up toward the free surface at $t = 0.042$ s.

The free surface and cavity at four time instants for the projectile model with a 90°, 120°, and 150° cone-shaped head in Cases 2, 3, and 4 are shown in Figs. 11, 12, and 13, respectively. It can be observed that open cavities were formed when the head entered the water. However, there are discrepancies for their cavity closures and the complicated free surface as a result of the limitations of 2-D simulations.

As shown in Figs. 11 and 12, the width of open cavities near the free surface was increased along with the increase of the depth of the projectile model in the water. For the lower bubbles near the bottom of the projectile model, the width of the cavity did not change violently and was close to the diameter of the cylinder. The geometry of the cavity for the projectile model with a small angle cone-shaped head was slenderer than that for the projectile model with a large angle cone-shaped head, which is presented in Fig. 13. For the cavity formed by the water entry of the projectile model with a 150° cone-shaped head, some water particles moved into the region of the cavity. The width of the upper and lower parts of the cavity was increased while it became narrow in the middle section.

The head shapes of the projectile also affected the deformation of the free surface. As shown in Fig. 10, small splashing water on the free surface was formed in the numerical results of the projectile with a hemispherical head, whereas it was not observed in the experimental snapshots in Case 1. In Figs. 11–13, the free surface was highly deformed and broken as a result of the impact of the projectiles with cone-shaped heads in Cases 2~4. Water was splashed on the free surface, which was different from the free surface for the projectile model with a hemispherical head. The splashed water particles could drop, and the interaction with air particles in the cavity flow could exist.

$t = 0.022$ s. When the length of the bubble was increased larger than the length of the projectile, the top part of the bubble tended to be compressed. The width of the upper side was decreased and smaller than the diameter of the cylinder. The bottom part of the
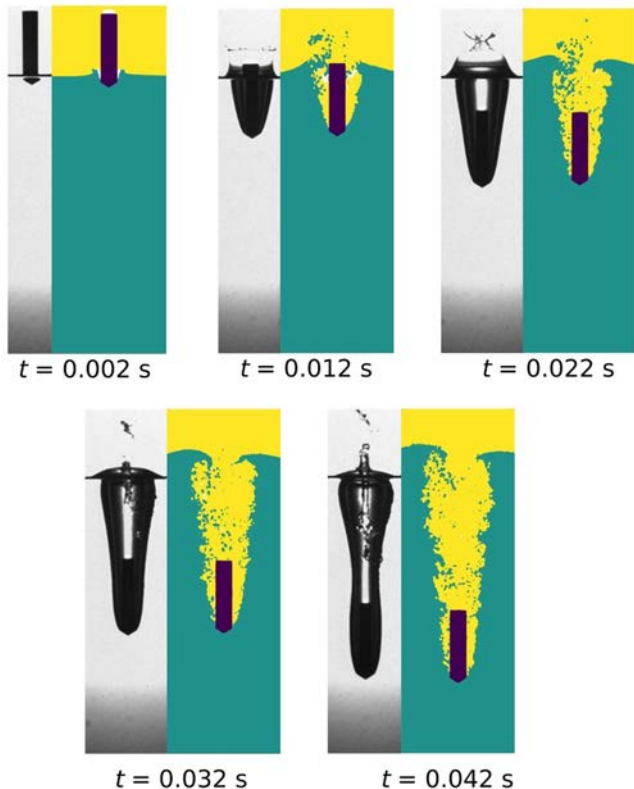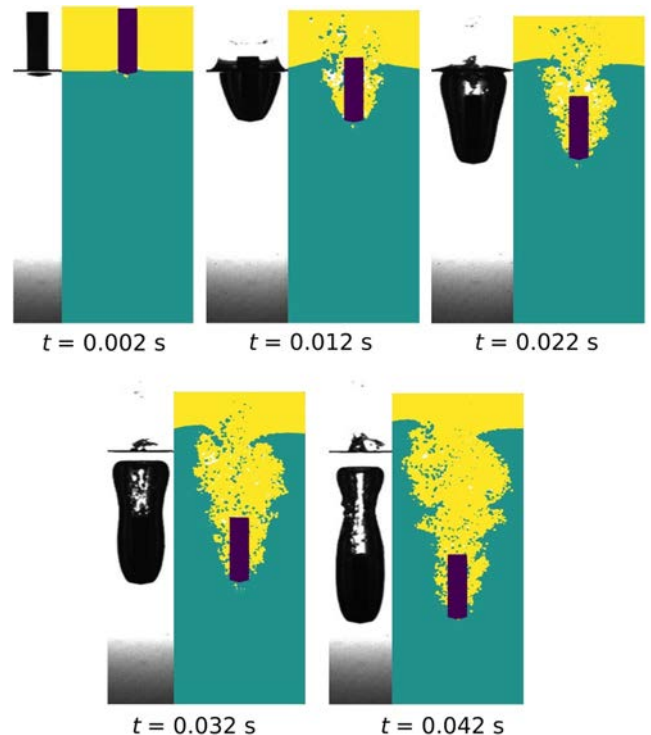

Fig. 12 Typical cavity geometries and free surface evolution during water entry of Model 3 with a 120° cone-shaped head

Fig. 13 Typical cavity geometries and free surface during water entry of Model 4 with a 150° cone-shaped head

(a) Model 1 (b) Model 2

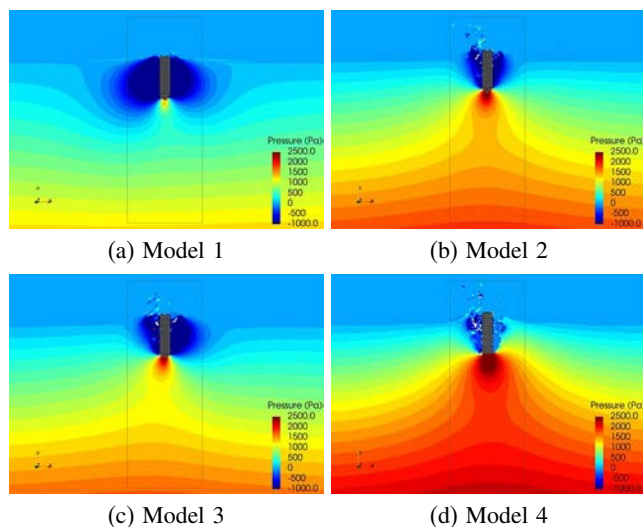(c) Model 3 (d) Model 4

Fig. 14 Comparison of the pressure fields of four projectiles at $t = 0.012$ s during water entry

(a) Model 1 (b) Model 2
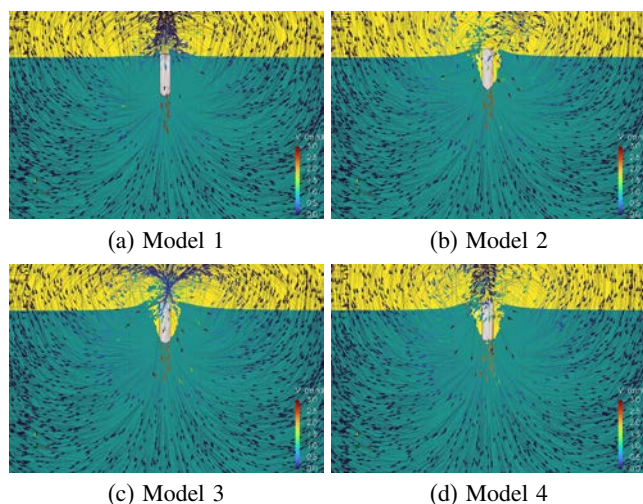
(c) Model 3 (d) Model 4

Fig. 15 Comparison of the velocity fields of four projectiles at $t = 0.012$ s during water entry

The snapshots of the pressure field and velocity field at $t = 0.012$ s are shown in Figs. 14 and 15, respectively. High pressure can be found near the head of the projectile. It can be observed that the impact pressure for Model 4 with a 150° cone-shaped head was the highest, whereas that for Model 1 with a hemispherical head was the lowest.

CONCLUSIONS

Projectiles with a hemispherical head and three cone-shaped heads with different angles entering the calm water were simulated by an improved multiphase MPS method. Convergence studies have been performed to examine sensitivities of vertical velocity and impact force to particle spacing and time step. The preliminary results of the corrected 2-D numerical predictions are generally in agreement with the experimental data. However, 3-D simulations are necessary to improve the numerical solutions. In terms of the effect of the head shape, a hemispherical head led to a smaller velocity loss and the cavity was free around the head during water entry. On the contrary, the cavity was generated near the head for the projectile with cone-shaped heads. The larger the angle of the cone-shaped head was, the greater velocity loss was

obtained. Cavity closures on the surface were observed for the projectile model with a hemispherical head, and the deep closure in the water was not included. In future work, 3-D simulations are necessary to analyze the motion of projectiles, the flow fields, and the cavity evolution for projectile entry into calm water with a low speed in detail.

REFERENCES

Duan, G, Koshizuka, S, and Chen, B (2015). "A Contoured Continuum Surface Force Model for Particle Methods," *J Comput Phys,* 298(C), 280–304.
https://doi.org/10.1016/j.jcp.2015.06.004.

Duan, G, Koshizuka, S, Chen, B, and Xiang, H (2017). "Stable Multiphase Moving Particle Semi-implicit Method for Incompressible Interfacial Flow," *Comput Methods Appl Mech Eng*, 318, 636–666. https://doi.org/10.1016/j.cma.2017.01.002.

Gong, K, Wang, B, and Liu, H (2011). "Modelling Water Entry of a Wedge by Multiphase SPH Method," *Coastal Eng Proc*, 1(32). https://doi.org/10.9753/icce.v32.waves.10.

Gotoh, H, Khayyer, A, and Shimizu, Y (2021). "Entirely Lagrangian Meshfree Computational Methods for Hydroelastic Fluid-structure Interactions in Ocean Engineering—Reliability, Adaptivity and Generality," *Appl Ocean Res*, 115, 102822. https://doi.org/10.1016/j.apor.2021.102822.

Jiang, Y, Li, Y, Guo, J, Yang L, and Wang, H (2021). "Numerical Simulations of Series and Parallel Water Entry of Supersonic Projectiles in Compressible Flow," *Ocean Eng*, 235, 109155. https://doi.org/10.1016/j.oceaneng.2021.109155.

Khayyer, A, and Gotoh, H (2013). "Enhancement of Performance and Stability of MPS Meshfree Particle Method for Multiphase Flows Characterized by High Density Ratios," *J Comput Phys,* 242, 211–233. https://doi.org/10.1016/j.jcp.2013.02.002.

Khayyer, A, and Gotoh, H (2016). "A Multiphase Compressible-incompressible Particle Method for Water Slamming," *Int J Offshore Polar Eng,* ISOPE, 26(1), 20–25.
https://doi.org/10.17736/ijope.2016.mk42.

Khayyer, A, Gotoh, H, and Shimizu, Y (2017). "Comparative Study on Accuracy and Conservation Properties of Two Particle Regularization Schemes and Proposal of an Optimized Particle Shifting Scheme in ISPH Context," *J Comput Phys*, 332, 236–256. https://doi.org/10.1016/j.jcp.2016.12.005.

Khayyer, A, Gotoh, H, and Shimizu, Y (2019). "A Projection-based Particle Method with Optimized Particle Shifting for Multiphase Flows with High Density Ratios and Discontinuous Density Fields," *Comput Fluids,* 179, 356–371.
https://doi.org/10.1016/j.compfluid.2018.10.018.

Khayyer, A, Gotoh, H, and Shimizu, Y (2022). "On Systematic Development of FSI Solvers in the Context of Particle Methods," *J Hydrodyn*, 34(3), 395–407.
https://doi.org/10.1007/s42241-022-0042-3.

Koshizuka, S, and Oka, Y (1996). "Moving-particle Semi-implicit Method for Fragmentation of Incompressible Fluid," *Nucl Sci Eng*, 123(3), 421–434.
https://doi.org/10.13182/NSE96-A24205.

Lee, BH, Park, JC, Kim, MH, and Hwang, SC (2011). "Step-by-step Improvement of MPS Method in Simulating Violent Free-surface Motions and Impact-loads," *Comput Methods Appl Mech Eng*, 200(9–12), 1113–1125. https://doi.org/10.1016/j.cma.2010.12.001.

Lee, M, Longoria, RG, and Wilson, DE (1997). "Cavity Dynamics in High-speed Water Entry," *Phys Fluids*, 9(3), 540–550. https://doi.org/10.1063/1.869472.

Liu, M, and Zhang, Z (2019). "Smoothed Particle Hydrodynamics (SPH) for Modeling Fluid-structure Interactions," *Sci China Phys Mech Astron*, 62, 984701. https://doi.org/10.1007/s11433-018-9357-0.

Luo, M, Khayyer, A, and Lin, P (2021). "Particle Methods in Ocean and Coastal Engineering," *Appl Ocean Res*, 114, 102734. https://doi.org/10.1016/j.apor.2021.102734.

Mirzaei, M, Taghvaei, H, and Alishahi, MM (2020). "Mathematical Modeling of the Oblique Water-entry of Cylindrical Projectiles," *Ocean Eng*, 205, 107257. https://doi.org/10.1016/j.oceaneng.2020.107257.

Monaghan, JJ (1988). "An Introduction to SPH," *Comput Phys Commun*, 48(1), 89–96. https://doi.org/10.1016/0010-4655(88)90026-4.

Nomura, K, Koshizuka, S, Oka, Y, and Obata, H (2001). "Numerical Analysis of Droplet Breakup Behavior Using Particle Method," *J Nucl Sci Technol*, 38(12), 1057–1064. https://doi.org/10.1080/18811248.2001.9715136.

Rezavand, M, Zhang, C, and Hu, X (2019). "A Weakly Compressible SPH Method for Violent Multi-phase Flows with High Density Ratio," *J Comput Phys*, 402, 109092. https://doi.org/10.1016/j.jcp.2019.109092.

Shakibaeinia, A, and Jin, Y-C (2012). "MPS Mesh-free Particle Method for Multi-phase Flows," *Comput Methods Appl Mech Eng,* 229–232, 13–26. https://doi.org/10.1016/j.cma.2012.03.013.

Shimizu, Y, Gotoh, H, and Khayyer, A (2018). "An MPS-based Particle Method for Simulation of Multiphase Flows Characterized by High Density Ratios by Incorporation of Space Potential Particle Concept," *Comput Math Appl*, 76(5), 1108–1129. https://doi.org/10.1016/j.camwa.2018.06.002.

Song, Z, Duan, W, Xu, G, and Zhao, B (2020). "Experimental and Numerical Study of the Water Entry of Projectiles at High Oblique Entry Speed," *Ocean Eng*, 211, 107574. https://doi.org/10.1016/j.oceaneng.2020.107574.

Sun, P, Le Touzé, D, Oger, G, and Zhang, A (2020a). "An Accurate SPH Volume Adaptive Scheme for Modeling Strongly-compressible Multiphase Flows. Part 1: Numerical Scheme and Validations with Basic 1D and 2D Benchmarks," *J Comput Phys*, 426(2), 109937. https://doi.org/10.1016/j.jcp.2020.109937.

Sun, P, Le Touzé, D, Oger, G, and Zhang, A (2020b). "An Accurate SPH Volume Adaptive Scheme for Modeling Strongly-compressible Multiphase Flows. Part 2: Extension of the Scheme to Cylindrical Coordinates and Simulations of 3D Axisymmetric Problems with Experimental Validations," *J Comput Phys*, 426, 109936. https://doi.org/10.1016/j.jcp.2020.109936.

Techet, AH, and Truscott, TT (2011). "Water Entry of Spinning Hydrophobic and Hydrophilic Spheres," *J Fluids Struct*, 27(5–6), 716–726. https://doi.org/10.1016/j.jfluidstructs.2011.03.014.

Truscott, TT, and Techet, AH (2009a). "A Spin on Cavity Formation During Water Entry of Hydrophobic and Hydrophilic Spheres," *Phys Fluids*, 21(12), 180. https://doi.org/10.1063/1.3272264.

Truscott, TT, and Techet, AH (2009b). "Water Entry of Spinning Spheres," *J Fluid Mech*, 625, 135–165. https://doi.org/10.1017/S0022112008005533.

Wen, X, Zhao, W, and Wan, D (2021a). "An Improved Moving Particle Semi-implicit Method for Interfacial Flows," *Appl Ocean Res*, 117, 102963. https://doi.org/10.1016/j.apor.2021.102963.

Wen, X, Zhao, W, and Wan, D (2021b). "A Multiphase MPS Method for Bubbly Flows with Complex Interfaces," *Ocean Eng*, 238(4), 109743. https://doi.org/10.1016/j.oceaneng.2021.109743.

Wen, X, Zhao, W, and Wan, D (2022). "Multi-phase Moving Particle Semi-implicit Method for Violent Sloshing Flows," *Eur J Mech B*, 95, 1–22. https://doi.org/10.1016/j.euromechflu.2022.04.002.

Yang, H, Zhang, A, Gong, X, and Yao, X (2014). "Experimental Study of the Cavity of Low Speed Water Entry of Different Head Shape Projectiles," *J Harbin Eng Univ*, 35(9), 1060–1066 (in Chinese). https://doi.org/10.3969/j.issn.1006-7043.201304035.

Zhang, G, Zhao, W, and Wan, D (2022). "Moving Particle Semi-implicit Method Coupled with Finite Element Method for Hydroelastic Responses of Floating Structures in Waves," *Eur J Mech B Fluids*, 95, 63–82. https://doi.org/10.1016/j.euromechflu.2022.04.005.

Zhang, Y, and Wan, D (2017). "Numerical Study of Interactions between Waves and Free Rolling Body by IMPS Method," *Comput Fluids,* 155, 124–133. https://doi.org/10.1016/j.compfluid.2017.03.019.